Supplement of Atmos. Meas. Tech., 8, 4055–4074, 2015
http://www.atmos-meas-tech.net/8/4055/2015/
doi:10.5194/amt-8-4055-2015-supplement

Atmospheric Measurement Techniques
Open Access

Supplement of

Development and characterisation of a state-of-the-art GOME-2 formaldehyde air-mass factor algorithm

W. Hewson et al.

Correspondence to: M. P. Barkley (mpb14@le.ac.uk)

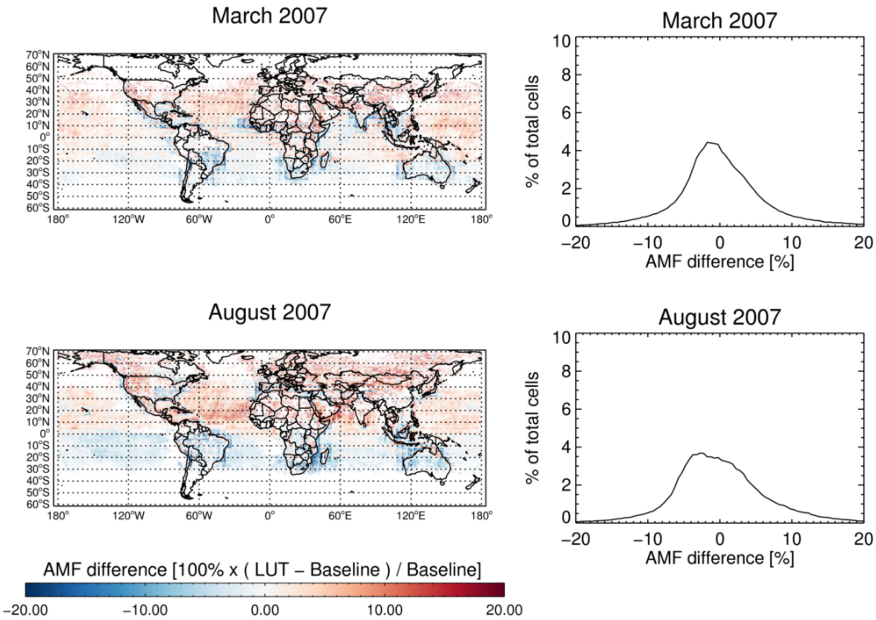

Figure 1: Left: spatial maps of the AMF differences, relative to the default UoL AMF baseline algorithm, resulting from the use of the look-up table (LUT) AMFs, as discussed in section 4.4 of the main text. AMFs are gridded on to $0.25° \times 0.25°$ using observations with cloud fractions $\leq 40\%$. Right: corresponding histograms of the AMF differences.

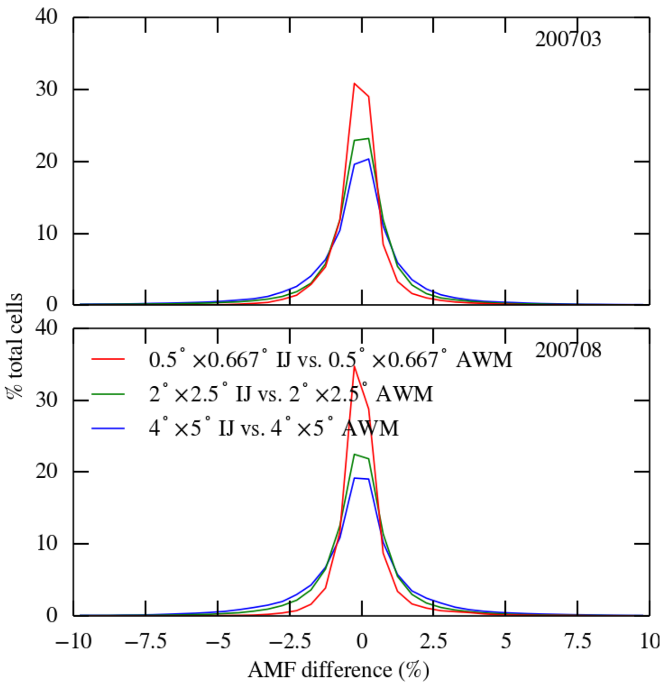

Figure 2: The relative AMF differences between the IJ and area-weighting (AWM) profile selection methods for each of the different GEOS-Chem model simulations ($4°\times5°$; $2°\times2.5°$; and $0.5°\times0.667°$), as discussed in section 5.3. For example, the green line represents $100\% \times (2°\times2.5°$ AWM $-$ $2°\times2.5°$ IJ) / $2°\times2.5°$ IJ, and so forth. The impact of area-weighting is generally small.

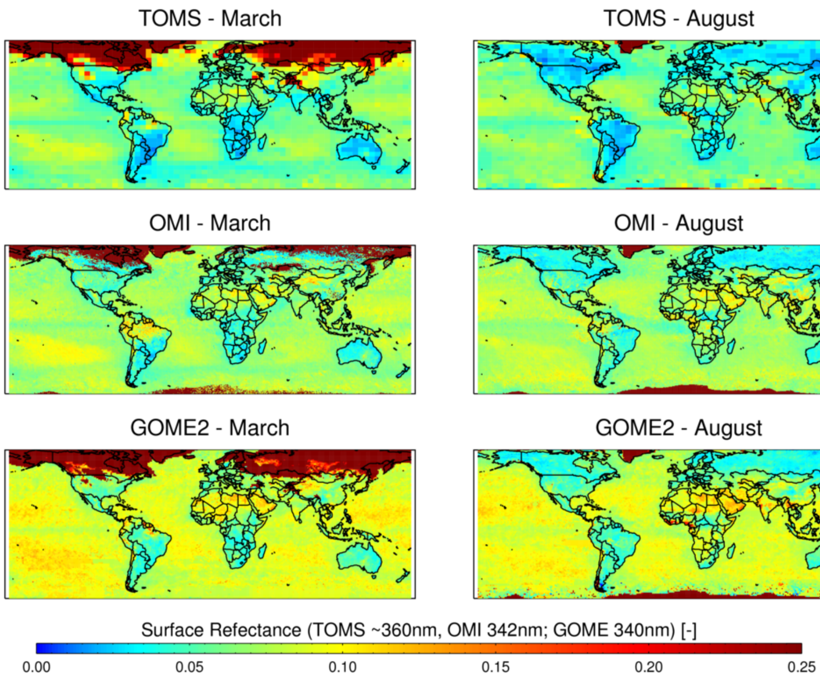

Figure 3: TOMS surface Lambertian-equivalent reflectance (LER) at a wavelength of ∼360 nm at 4°×5° resolution (Herman and Celarier, 1997), OMI mode LER at 342 nm at 0.5°×0.5° resolution (Kleipool et al., 2008) derived from 5 years of OMI observations, and GOME-2 mode LER at 340 nm at 1.0°×1.0° resolution (Tilstra et al., 2014), for March (left) and August (right). Note colour bar saturates at 0.25 to resolve lower value albedos.

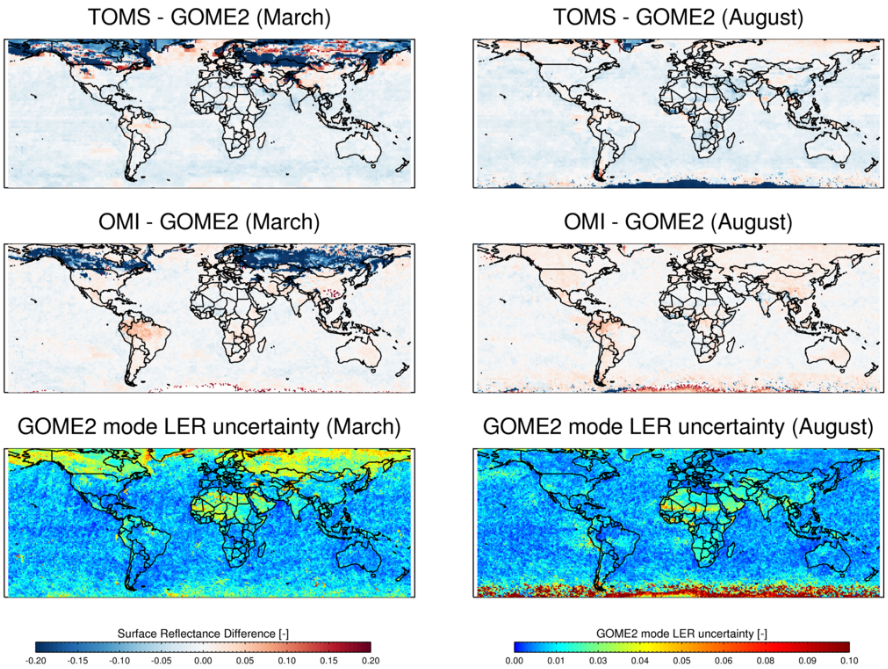

Figure 4: The surface reflectance differences between the GOME-2 340 nm mode surface Lambertian-equivalent reflectance (LER) and the TOMS LER ($\sim$360 nm) and OMI 342 nm mode LER (both hregridded to $1^\circ\times1^\circ$ resolution matching the GOME-2 LER data), for March (left) and August (right). The GOME-2 340 nm mode LER uncertainty is shown in the lower two plots. The correlation of the GOME-2 340 nm mode LER uncertainties with the surface reflectances differences are weak $|r| < 0.4$.

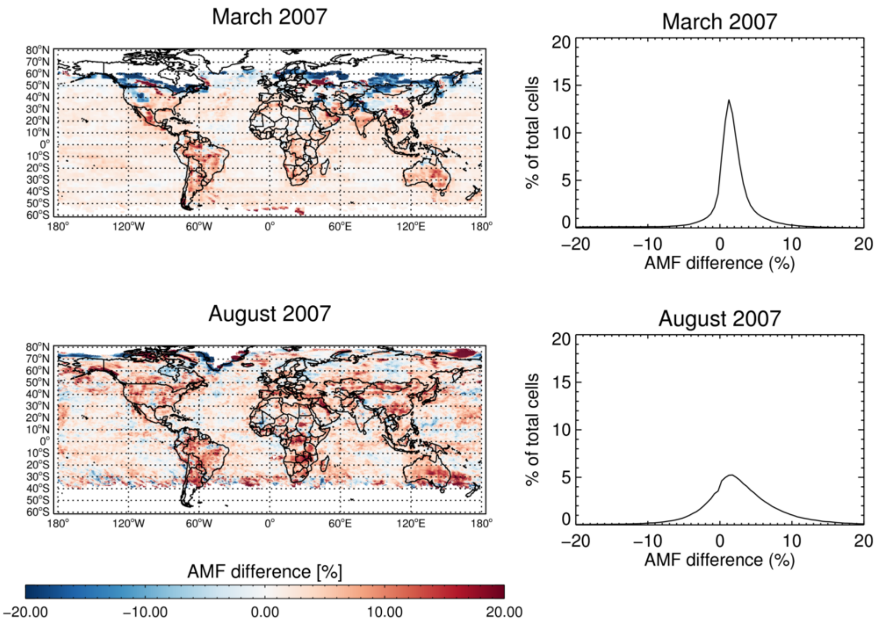

Figure 5: Left: spatial maps of the AMF differences, relative to the default UoL AMF algorithm, resulting from the use of the temporally interpolated and area-weighted OMI 0.5°×0.5° 342 nm mode surface Lambertian-equivalent reflectance (LER) (Kleipool et al., 2008), as discussed in section 5.5. AMFs are gridded to 0.25°×0.25° using observations with cloud fractions ≤40%. Right: corresponding histograms of the AMF differences are shown in blue.

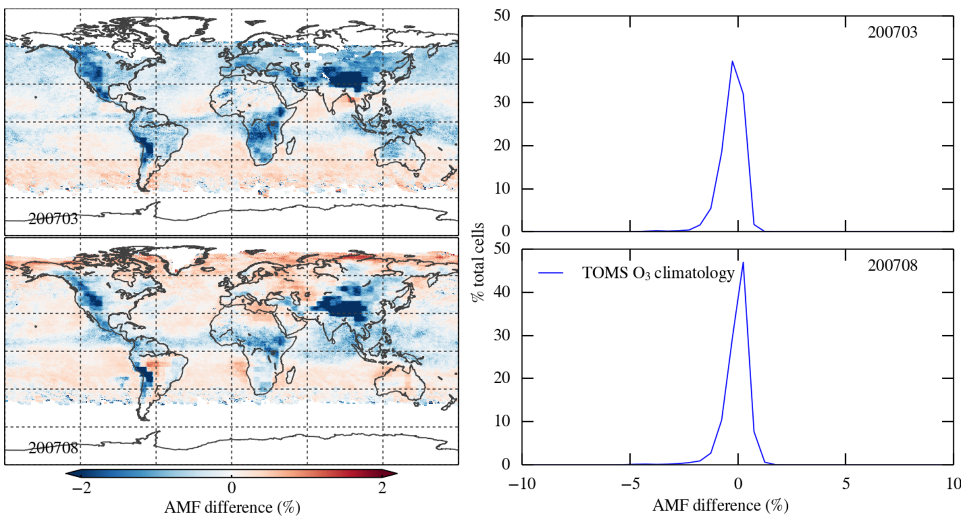

Figure 6: Left: spatial maps of the AMF differences, relative to the default UoL AMF algorithm, resulting from the use of the TOMS ozone climatology, as discussed in section 5.7 of the main text. AMFs are gridded on to $0.25° \times 0.25°$ grid using observations with cloud fractions $\leq 40\%$. Right: corresponding histograms of the AMF differences are shown in blue.

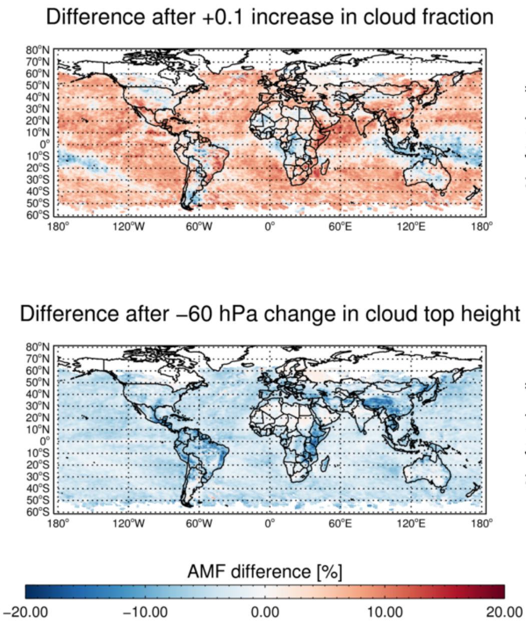

Figure 7: Global maps (left) and histograms (right) of the change in the March 2007 AMFs from increasing the cloud fraction by +0.1 (top) and cloud-top height by −60 hPa (bottom), in the final updated AMF algorithm. AMF differences are gridded on to a $0.25^{\circ} \times 0.25^{\circ}$ grid using observations with cloud fractions $\leq 40\%$.

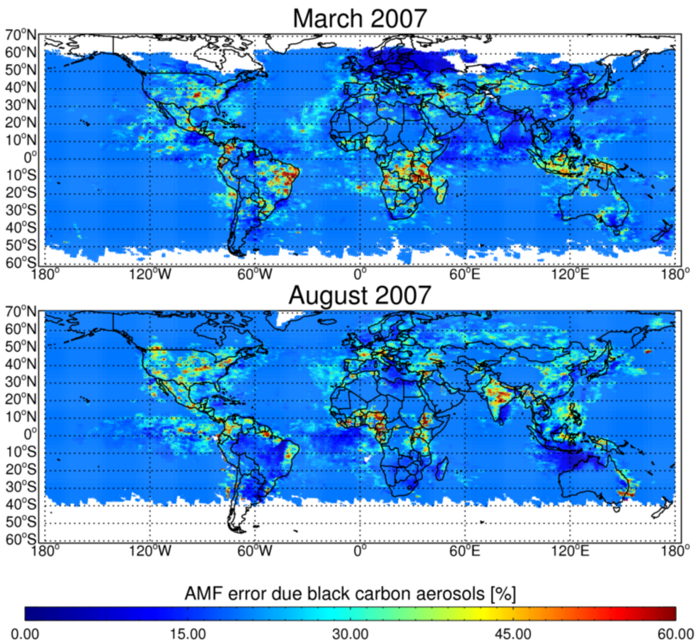

Figure 8: Additional black carbon AMF errors for March 2007 (top) and August 2007 (bottom) as described in section 6.1. AMF errors are gridded on to a 0.25°×0.25° grid using observations with cloud fractions ≤40%.

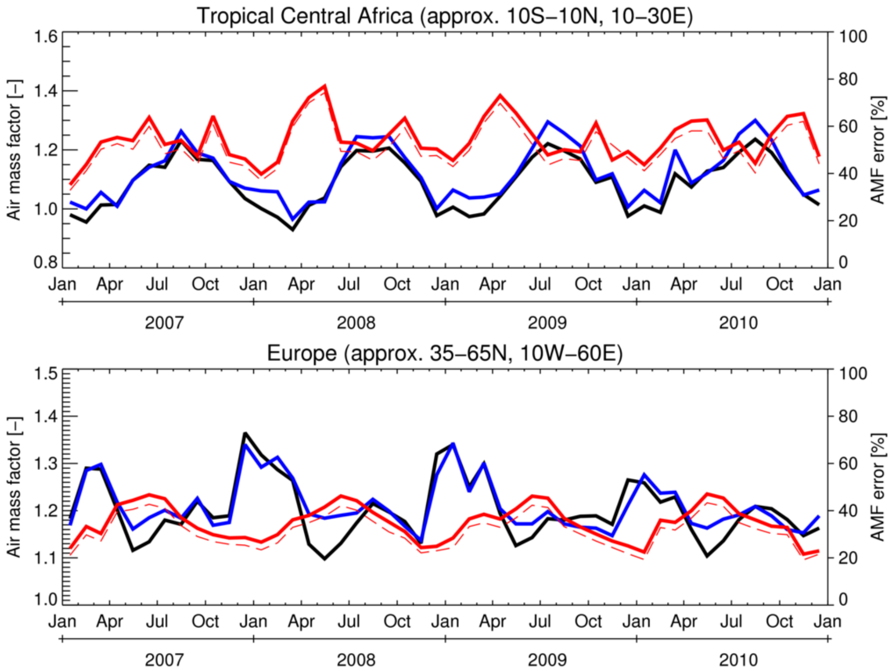

Figure 9: 2007–2010 time series over tropical central Africa (top) and Europe (bottom), showing monthly median AMFs calculated with and without aerosols (solid black and blue lines, respectively), and monthly median total AMF error (red solid line; calculated with aerosols present). The dashed red line shows the contribution to the total AMF error from uncertainty in the HCHO profile shape.